JOURNAL OF GEOPHYSICAL RESEARCH, VOL. 114, B12303, doi:10.1029/2008JB005998, 2009

High-resolution onshore seismic imaging of complex volcanic structures: An example from Vulcano Island, Italy

Pier Paolo G. Bruno[1,2] and Antonio Castiello[3]

Received 8 August 2008; revised 23 May 2009; accepted 5 August 2009; published 5 December 2009.

[1] Detailed seismic images of subsurface structures of volcanic calderas are fundamental to improve the structural and volcanological knowledge of these high-risk volcanoes. However, high-quality seismic data are difficult to obtain in volcanic areas, especially on shore. We report the results of a high-resolution seismic profiling of the western sector of La Fossa Caldera (Vulcano Island, Italy). Using a high-resolution vibrating source and both alternative acquisition and processing techniques, we were able to overcome most of the inconvenience caused by volcanic lithotypes. This study provides the subsurface distribution of volcanic deposits as well as the recognition of some significant intracaldera structures. We located a parasitic vent or hyaloclastite mound buried under La Fossa Caldera, which is dissipating CO_2 in an area where earthquakes have been recorded at about 1 km depth. Furthermore, the deformation pattern found at the southernmost part of the profile is consistent with a caldera collapse after a dome intrusion. The results suggest that the use of high-resolution vibrating sources combined with alternative seismic acquisition techniques and nonconventional processing could help to recover detailed information on the shallow structures of volcanic areas.

Citation: Bruno, P. P. G., and A. Castiello (2009), High-resolution onshore seismic imaging of complex volcanic structures: An example from Vulcano Island, Italy, *J. Geophys. Res.*, *114*, B12303, doi:10.1029/2008JB005998.

1. Introduction

[2] Achievement of high-quality, high-resolution seismic data in a volcanic environment can prove extremely difficult. This limitation is not new, and in spite of significant operational efforts, conventional seismic reflection techniques commonly deliver poor quality in volcanic environments because of diffraction and scattering, attenuation, and static problems [*Dell'Aversana et al.*, 2000]. This problem is particularly true on shore because of the lack of a homogeneous water layer which allows an efficient transmission of the seismic energy. For example, in onshore volcanic environments, the assumption of laterally homogeneous media (used in standard velocity analysis) fails even at short two-way traveltime (TWT), causing degradation of common midpoint (CMP) stacking and inaccurate background velocity models for migration techniques [e.g., *Jin and Madariaga*, 1994]. Moreover, high-resolution seismic reflection data are plagued by the overwhelming effects of direct, refracted, guided, and surface waves. These different components of source-generated noise may completely mask reflections at traveltimes <50–100 ms [*Roth and Holliger*, 1999]. One of the aims of this paper is to show that the use of alternative field data acquisition techniques and instruments and alternative processing can get through the difficulties affecting reflection seismology in onshore volcanic settings and can improve the reflection data imaging of the near surface.

[3] The success of swept sources for petroleum exploration has led to the recent development of high-frequency vibrators as a valid alternative to the impulsive sources commonly used in shallow seismic reflection work. Several papers describe the use of vibratory sources for exploration of igneous structures. For example, *Kasahara et al.* [1991] and *Reshef et al.* [2003] used vibratory sources to improve the imaging of the top basalt layer in the eastern coast of the Izu Peninsula (Japan). *Hammer et al.* [2004] utilized vibrating seismic sources to resolve thin, diamondiferous kimberlite dikes from the surface to depths greater than 1300 m. Here we present one of the first attempts at detailed seismic reflection imaging of an active caldera using a high-resolution vibrating seismic source. Because the survey was acquired in a sensitive environment, only noninvasive sources could be considered. Following *Doll et al.* [1998], we use the term "noninvasive" to refer to sources that do not require or result in penetration of the ground surface with an auger, projectile, or other device. Noninvasive techniques are generally preferred at sensitive sites because they do not add contaminants that are regulated (e.g., lead) or create new migration paths for contaminants. The Minivib® vibroseis used in this experiment has proven to be one of the most effective high-resolution sources for shallow reflection surveys [*Doll et al.*, 1998]. Our seismic experiment was done at Vulcano Island, one of the highest-risk volcanoes in

[1]Sezione Osservatorio Vesuviano, Istituto Nazionale di Geofisica e Vulcanologia, Naples, Italy.
[2]Formerly at Department of Exploration Geophysics, Curtin University, Kensington, Western Australia, Australia.
[3]Sezione Sismologia e Tettonofisica, Istituto Nazionale di Geofisica e Vulcanologia, Rome, Italy.

0148-0227/09/2008JB005998$09.00

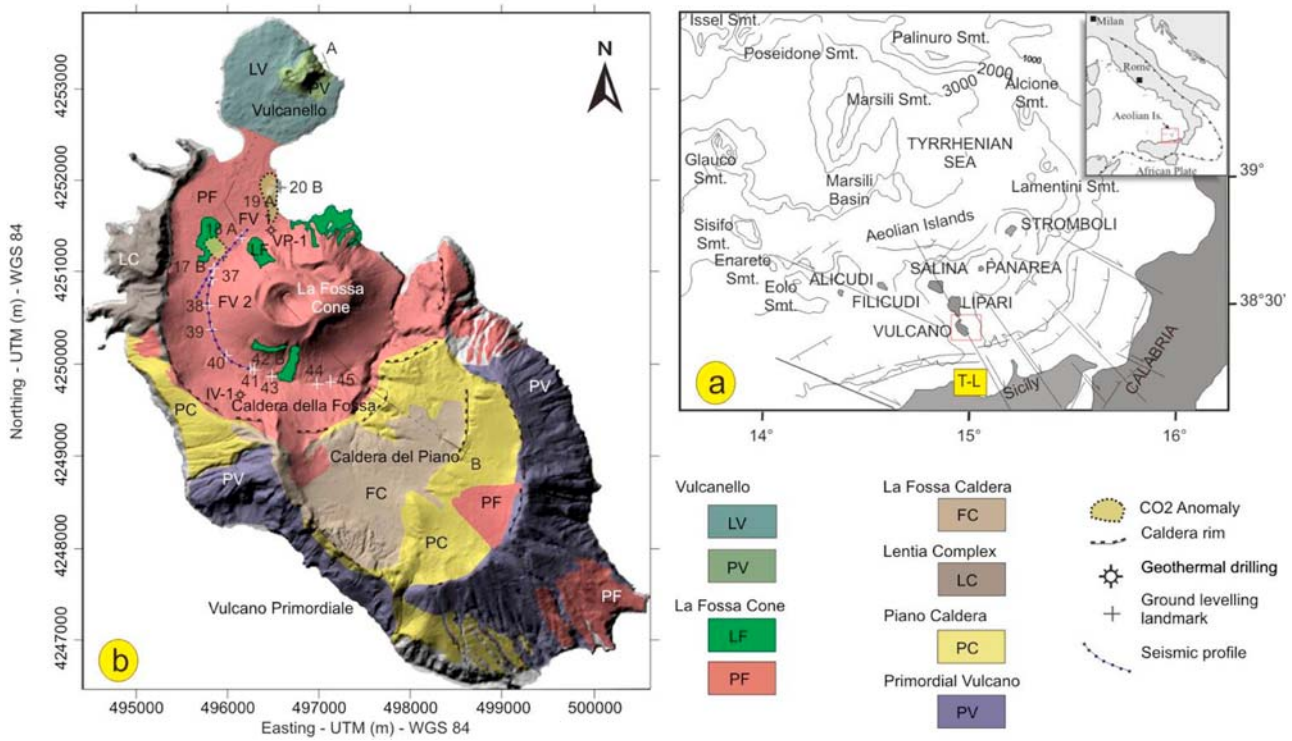

Figure 1. (a) Sketch of the Aeolian archipelago with main structural features modified from *Finetti and Del Ben* [1986]. T-L is the Tindari-Letojanni fault alignment. Main seamounts are also shown. (b) Schematic geological map (modified from *Okuma et al.* [2006], *De Astis et al.* [1997], and *Gioncada et al.* [2003]) plotted over a digital terrain model image of Vulcano Island [*Baldi et al.*, 2000]. LV, Vulcanello lavas; PV, Vulcanello pyroclastics; LF, La Fossa Cone lavas; PF, La Fossa Cone pyroclastics; FC, Fossa Caldera, products and volcanic units; LC, Lentia Complex, lava flows and domes; PC, Piano Caldera, in-fill products and volcanic units; PV, Primordial Vulcano. Line A-B is the trace of geological cross section of *De Astis et al.* [2006]. IV1 and VP1 are the AGIP-ENEL-EMS drilling locations. The high CO_2 flux anomalous area [*Diliberto et al.*, 2002] is also shown as dotted, green-filled curves.

Italy. Here we acquired two seismic profiles (FV1 and FV2) at the western flank of Gran Cono (last eruption in 1889–1890) within La Fossa Caldera (Figures 1b and 2). In this area, volcanological studies suggested the presence of a complex and still-active shallow magmatic feeding system [e.g., *De Astis et al.*, 1997]. Other recent evidences of activity at La Fossa Caldera include (1) strong periodical increases of fumarole temperature [*Granieri et al.*, 2006] and (2) shallow depth (<2 km) earthquakes within the caldera [*Privitera*, 1997]. In light of these evidences, La Fossa may represent an area with high probability of renewal of volcanic activity. At Vulcano we used a new high-resolution seismic reflection strategy, which combines both alternative acquisition and processing techniques and surmounts many of the traditional problems identified above [*Dell'Aversana et al.*, 2000].

[4] Field operation improvements for deep and oil exploration surveys in complex terrains are the "wide-angle reflection-refraction" [e.g., *Makris and Thiessen*, 1984] and the "global offset" [*Dell'Aversana et al.*, 2000]. The general idea behind these techniques is to extend the distance range of seismic observations in order to get additional constraints on the reflector shape and position using first arrival traveltime tomography. For example, a global offset layout, used by *Dell'Aversana et al.* [2000] for crustal-scale exploration, consists of a conventional split-spread seismic reflection recording array moving with the source and merged with a wide-aperture array made by fixed stand-alone units placed along the profile and used for nonlinear tomographic inversion of first arrivals. This technique was modified by *Improta and Bruno* [2007] for high-resolution shallow imaging of active faults in complex terrains. Global offset strategy allows us to utilize advanced imaging techniques such as traveltime and full waveform tomographic inversion and prestack depth migration [*Operto et al.*, 2004]. Unfortunately, the larger spacing of the stand-alone units with respect to the reflection array makes it difficult to handle both data sets by conventional seismic reflection techniques [see *Improta and Bruno*, 2007].

[5] For our acquisition, we used a "wide-aperture" acquisition layout that, unlike the standard "global offset" technique, is based on a regular and densely spaced (5 m) geophone spread with a length of 475 m, which is greater than the maximum expected depth of interest (~200 m). Regularly spaced geophone spreads lead to constant and small CMP spacing, which is more appropriate for seismic reflection data processing. Furthermore, the layout is large enough to allow using first arrival tomography for improving the reliability of the static corrections and for CMP stacking

Figure 2. Photograph of the southeastern sector of La Fossa Caldera showing the Minivib during the acquisition of seismic profile FV2. Rough logistical conditions characterize the site; the soil is made up by dry and loose variable size sediments reworked from outcropping pyroclastic flows, fall, and lava beds. Visible on the right is La Fossa Volcano and, in the background at left, the northern boundary of La Fossa Caldera with Lentia Complex and Vulcanello (LC and LV in Figure 1).

of the shallowest reflectors. Tomography data are also used in this paper to extend and to complement the seismic imaging at the very near surface (first 30–50 m deep).

2. Geological Background

[6] The Aeolian Archipelago is located in the southeast sector of the Tyrrhenian Sea and comprises seven volcanic islands (Alicudi, Filicudi, Salina, Lipari, Vulcano, Panarea, and Stromboli, from west to east). The subaerial volcanoes of the Aeolian Arc and the associated volcanic seamounts form a ring-shaped structure emplaced on a thinned (about 20 km) continental crust. Here volcanic activity is thought to originate from the subduction of the African plate beneath the European plate at the southern edge of the Tyrrhenian Sea [*Furukawa et al.*, 2001]. In this geodynamic framework the Aeolian Islands are interpreted as a volcanic arc, and the Tyrrhenian Plain is a back-arc basin [*Keller*, 1974; *Barberi et al.*, 1994; *De Astis et al.*, 1997]. Vulcano Island is the southernmost side of a NW-SE structural alignment (see "T-L" in Figure 1a) that represents the surface expression of a dextral strike-slip fault system named Tindari-Letojanni, which is considered by some authors as the northward propagation of the Malta Escarpment, a lithospheric structure bounding the eastern margin of Sicily [e.g., *Continisio et al.*, 1997; *Ghisetti*, 1979]. The surface faults surveyed at Vulcano follow three main strikes: a prevailing NNW-SSE to NW-SE strike and second-order N-S and NE-SW strikes. The N-S and NE-SW striking faults, which splay out from the main strike-slip segments, show normal movements and represent tensional structures associated with the Tindari-Letojanni shear zone [*Frazzetta et al.*, 1982; *Ventura*, 1994]. Several volcanic complexes form the island of Vulcano (Figure 1b). Volcanological studies [e.g., *Keller*, 1980; *Castellet y Ballarà et al.*, 1982] indicate that subaerial volcanism at Vulcano migrated from the SSE to NNW sector, forming four main eruptive centers (from oldest, Primordial Vulcano, Lentia Complex, La Fossa Cone, and Vulcanello) and two calderas (Piano Caldera and La Fossa Caldera). The Primordial Vulcano is a truncated composite cone that forms the oldest (120–100 ka) and southernmost part of the island. It consists of alternating lava flows; scoriae deposits; and minor, fine-grained pyroclastic units. The Piano Caldera was formed (98 ka B.P.) by the collapse of the summit part of the Primordial Vulcano. Lentia Complex is a remnant of a larger structure sited north of Primordial Vulcano. It was formed between 24 and 15 ka, and it is cut by the western ring faults of La Fossa Caldera. La Fossa Caldera was emplaced by multiple collapses affecting the northern sector of the Piano Caldera and the Lentia Complex during the past 50 ka [*Gioncada and Sbrana*, 1991]. The present floor of the depression shows an altitude ranging from 0 m (northern sector) to 172 m (southern sector). La Fossa Caldera infill deposits erupted between 15 and 8 ka and consist of several pyroclastic and effusive units [*Gioncada and Sbrana*, 1991]. La Fossa Cone has grown inside La Fossa Caldera depression; the subaerial part is a composite tuff cone with minor lava flows emplaced in the past 6 ka, which rest on the compound lava flows of La Roia [*Frazzetta et al.*, 1983]. The Vulcanello Peninsula formed between the second century B.C. and the sixteenth century A.D. in the northern sector of the island.

[7] The Vulcano rocks belong to the high-K calc-alkaline, shoshonitic, and alkaline (potassic) associations [*Barberi et al.*, 1973; *Keller*, 1982]. This compositional range reflects the influence of the volcano-tectonic evolution on the Vulcano plumbing system [*De Astis et al.*, 2000]. The postcaldera magmas of La Fossa (15–8 kyr) show a complex active system of shallow magmatic feeding, consisting of a deep mafic magma chamber, which fed several small-sized shallow reservoirs [*De Astis et al.*, 1997]. The products of recent activity, concentrated at La Fossa and Vulcanello, indicate that the volume of the shallow reservoir is decreasing [*De Astis et al.*, 1997]. Periodical and sudden temperature increases at fumaroles and occurrences of shallow depth earthquakes (<2 km) at Piano Caldera and La Fossa Caldera might forecast future volcanic activity in this area [e.g., *Privitera*, 1997].

[8] Vulcano Island, for both its geodynamic role and its structural position along the Tindari-Letojanni alignment, has been targeted in the past by numerous geochemical and geophysical surveys. All data clearly demonstrate the existence of an active feeding system underneath the whole island, predominantly beneath the La Fossa Caldera [i.e., *Chiodini et al.*, 1992; *Berrino*, 2000]. In 1999, a high-resolution aeromagnetic survey, conducted by the Geological Survey of Austria, allowed the publication of the first

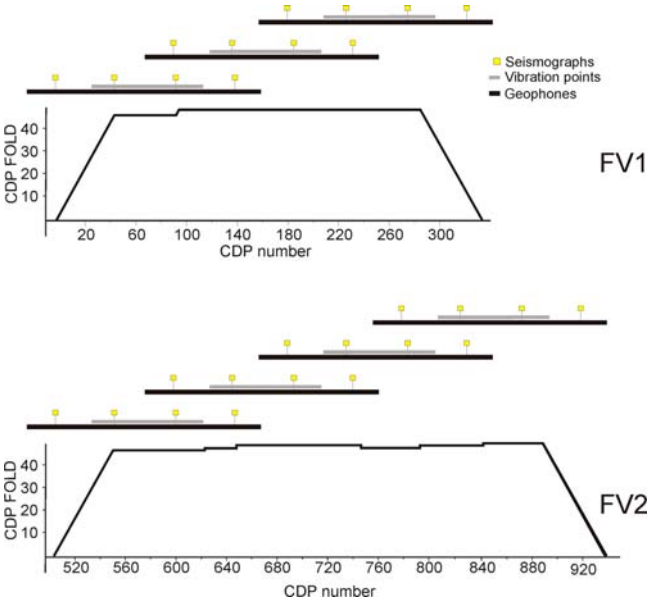

Figure 3. Pattern of "wide-aperture" acquisition geometry and relative CDP folding. FV1 and FV2 are characterized by three and four overlapping receiver spreads, respectively. The maximum CDP fold for both profiles is 48; the overlapping area is 48 channels.

detailed magnetic anomaly map of Vulcano and southern Lipari [*Supper et al.*, 2004]. *Blanco-Montenegro et al.* [2007] conducted another high-resolution aeromagnetic survey over the northern part of the island. They interpreted the presence of some positive magnetic anomalies at Piano Caldera as linked to the feeding system of the Primordial Vulcano phase and to the presence of a buried dike system intruded along intracaldera faults. *Diliberto et al.* [2002] identified two areas with anomalous high CO_2 fluxes at the foot of the volcanic cone of La Fossa (Figure 1b). According to Diliberto et al., those anomalies are due to degassing of a cooling magma body. *Revil et al.* [2008] conducted a survey of the inner structure of La Fossa Vulcano by high-resolution electric resistivity tomography coupled with self-potential, temperature, and CO_2 diffuse degassing measurements. These measurements provide an idea of the architecture of the edifice, including the geometry of the ash, tuff, and lava flow units and the spatial organization of the hydrothermal system. One of Revil et al.'s electric profiles (i.e., profile 4) is coincident with our seismic profiles. Unfortunately, saltwater contamination of the shallow subsurface of La Fossa Caldera made electric profiling ineffective at this site, and no useful data comparison could be done.

3. Data and Methods

[9] The total length of the seismic survey is about 2200 m (FV1, 955 m; FV2, 1195 m; Figures 1 and 4). A 300 m overlap between FV1 and FV2 allowed the achievement of an almost continuous image for about 1900 m. The basic acquisition configuration was similar for both FV1 and FV2 (Figure 3). The seismic profiles were recorded using four 24-bit, 24-channel engineering seismographs and 96 vertical geophones with an eigenfrequency of 10 Hz, placed at 5 m intervals. Source moveout was also 5 m. At each shot location we stacked three uncorrelated 10–150 Hz upsweeps of 12 s duration. The acquisition parameters, summarized in Table 1, allowed a maximum CMP redundancy of 4800%. The southern part of profile FV2 (Figure 1b) was in part acquired over a waste dump, which further decreased data quality. In addition to the above problems, for logistic reasons line FV2 was acquired and processed as a crooked line (Figure 4). From the processing point of view, crooked lines require more specialized processing than 2-D straight lines. More attention needs to be paid to the geometry, selection of stacking lines, and binning of the data.

[10] Shot records were acquired uncorrelated with the sweeps stored as auxiliary trace. Figure 5 shows two representative examples of raw common shot gathers (CSGs) after removal of the embedded sweep, which is traditionally completed by cross correlation of the trace with the sweep. However, this operation creates a zero-phase Klauder wavelet that is embedded in the data. Since the Earth behaves as a minimum phase filter, cross correlation of the trace (containing the Earth filter effect) with the sweep produces a mixed phase wavelet that causes a bad performance of some important processing algorithms, such as deconvolution. To avoid this problem, we used a frequency domain sweep deconvolution (FDSD) [*Brittle*, 2001] that removes the embedded sweep in the frequency domain by dividing the trace by the sweep. In Figure 5b, it can be seen that source-generated noise, mainly as surface waves, completely masks signals at traveltimes greater than 300–400 ms. Attenuation of coherent noise while preserving body waves is a difficult goal to achieve in land data processing. Conventional processing methods that include application of mute functions may lead to the misprocessing of source-generated noise as reflected events and/or to the unintentional removal of important shallow reflections. To remove source-generated noise, we used a combined linear and hyperbolic $\tau - p$ processing scheme, described by *Spitzer et al.* [2001], that results in the effective separation of reflections from source-generated noise. Figure 5a shows the effect of coherent noise removal on raw data, which allowed us to unmask the shallow reflectors.

[11] Basically, the subsequent processing was subdivided in three main phases: (1) deconvolution, (2) velocity analysis, and (3) migration. To minimize contamination of reflected energy with high-amplitude coherent noise, we applied an automatic gain control (AGC) to each shot panel. The AGC windows used were of 300 ms for prestack data and of 50 ms for stacked data. Deconvolution performance improved after the application of FDSD and minimum phase conversion; both minimum phase spiking and predictive deconvolution were used to raise the frequency of the signal and to minimize the reverberations and multiples.

[12] Static corrections are crucial to provide a better definition of reflected signals, particularly in the shallowest portion. Elevation along profiles ranges from 16.5 to 40 m above sea level (asl) for FV1 and from 44.5 to 69.5 m asl for FV2 (see Figures 6–8). For both lines a datum of 20 m asl was used. We used the refraction seismic tomography to calculate the replacement velocity for all receiver and source locations. Average total static shifts were ~ -32 ms and -66 ms for FV1 and FV2 with maximum shifts of -55 and -84 ms, respectively (see Figures 7 and 8). Residual

Table 1. Geometry and Recording Parameters Used During Acquisition of Seismic Profiles FV1 and FV2

	FV1 Line	FV2 Line
Geometry parameters		
Length	955 m	1195 m
Seismic source	IVI Minivib	IVI Minivib
Geophone interval	5 m	5 m
Shot spacing	5 m	5 m
Receiver spread size	96 geophones over 475 m (1 phone/group)	96 geophones over 475 m (1 phone/group)
Overlapping spreads	3	4
Minimum/maximum offset	2.5–357.5 m	2.5–357.5 m
Recording parameters		
Sweep characteristics	Linear 3 × 12 s upsweep from 10 to 200 Hz	Linear 3 × 12 s upsweep from 10 to 200 Hz
Sampling rate	1 ms	1 ms
Record length	14 s	14 s
Geophone	10 Hz vertical	10 Hz vertical

statics were also applied. For refraction data analysis over 31,000, first-arrival traveltimes were accurately hand-picked on the CSG and checked for consistency following *Ackermann et al.* [1986]. First-break picking of vibroseis data is known to be troublesome mainly because of the precursory events that parallel the true first break [*Mazzotti et al.*, 2000]. However, modern vibratory sources with control accelerometers mounted on the base plate (as with the high-resolution Minivib) allow a more reliable recording of source signatures, which can ultimately be used to improve first-break picking. For example, in our data, precursory events were attenuated by substituting FDSD to the cross correlation during preprocessing [*Brittle*, 2001; *Larsen et al.*, 2007]. In particular, FDSD allows avoiding sidelobe spurious reflectivity generated by the Klauder wavelet.

[13] Uncertainty on traveltime readings ranges from 1.25 ms (i.e., one eighth of the dominant period of the *P* pulse) to 12–15 ms depending on the offset. For traveltime propagation we used a "shortest-raypath" propagation method, where seismic raypaths can be found by calculating the shortest traveltime path through a node network, where node connection is based on a graph template [*Nakanishi and Yamaguchi*, 1986]. Data inversion was achieved by a nonlinear least squares approach [*Scales*, 1987]. The code accounts for nonlinearity by adding a variable damping parameter in the Gauss-Newton method. The 2-D starting models were determined via traditional refraction analysis procedures using traveltime curves from several source locations within the spreads. The inversion process is halted after 15 inversion runs. The finals models have RMS traveltime residuals equal to 2.36 and 4.12 ms for FV1 and FV2, respectively. Checkerboard tests performed using a sinusoidal perturbation pattern with cell size of 40 × 20 m and 20 × 10 m and extreme values of ±10% of final models (Figure 6) reveal that resolution of the velocity image rapidly deteriorates with depth according to ray penetration. The model is well-resolved down to about 40 m from the surface but provides valuable information on the shallower structure as it complements the seismic reflection gap at the surface.

[14] Integration of tomography (at lower TWT) and semblance (at higher TWT) was used to calculate the stacking velocities. For semblance analysis, we produced 20 panels, each one combining 31 common depth point reflections (CDPs) to obtain a densely spaced and accurate velocity analysis. Velocities range on average from about 900 m/s at the shallowest portion up to about 1600–1800 m/s at the deepest portion. These are average values. It is not uncommon to find higher or lower values.

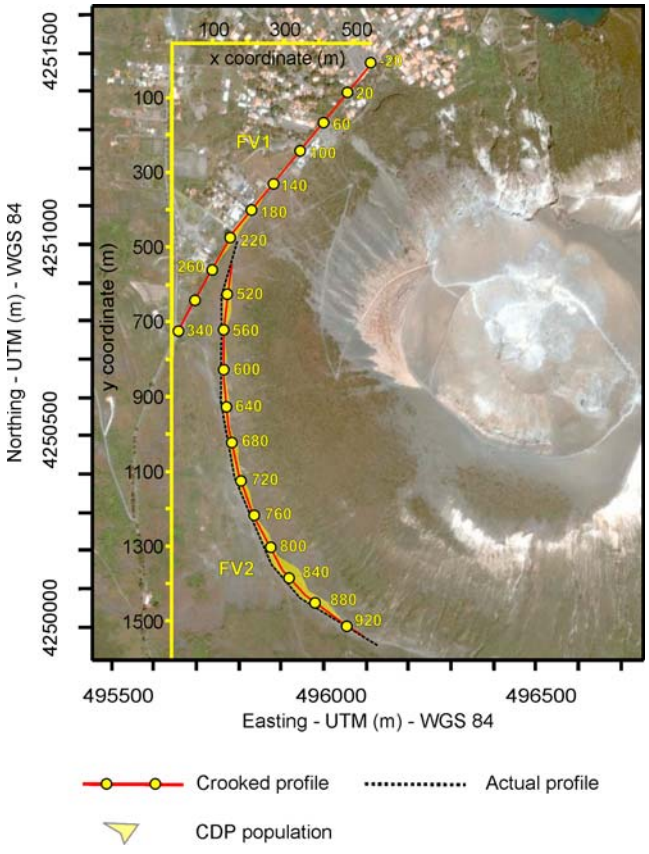

Figure 4. Illustration of crooked line geometry with X and Y coordinates in meters on satellite photography. The black dashed line is the survey station line. The red line is the processing line. The yellow dots are the CDP numbers of the processed line. The yellow area represents the spread of the midpoints. Google Earth imagery © Google Inc. Used with permission.

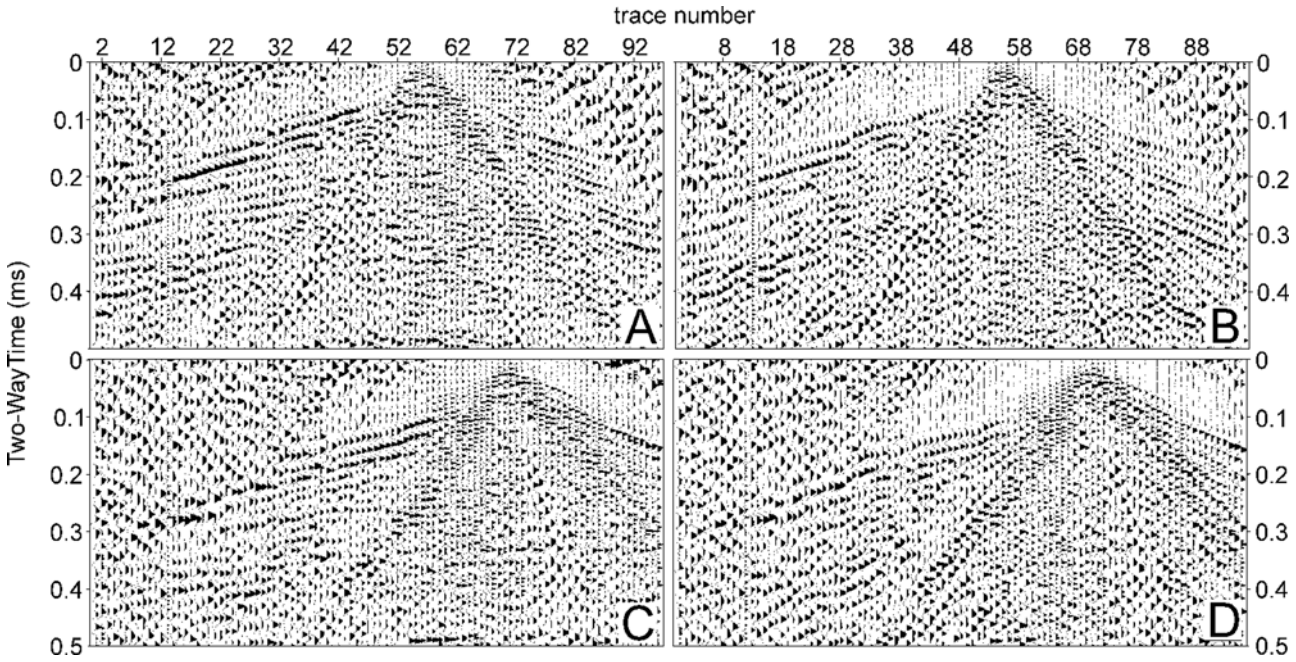

Figure 5. (a and c) Field shot gathers after $\tau - p$ source-generated noise removal. (b and d) Raw shots. Significant improvements in the quality of reflections in the shot gathers are readily apparent after $\tau - p$ filtering.

There are also several velocity inversions, not rare in volcanic terrains (i.e., CDP 220, FV1, in Figure 6).

[15] The first poststack process applied was the eigenvector filter. It uses the Karhunen theory [*Karhunen*, 1984] to decompose the data traces into eigenimages through the use of eigenvectors. The choice of which eigenimages are used in reconstruction allows for including or excluding types of seismic events or noise. This process may be thought of as a band pass over the eigenimage range. Random noise was removed from input data with eigenimage reconstruction

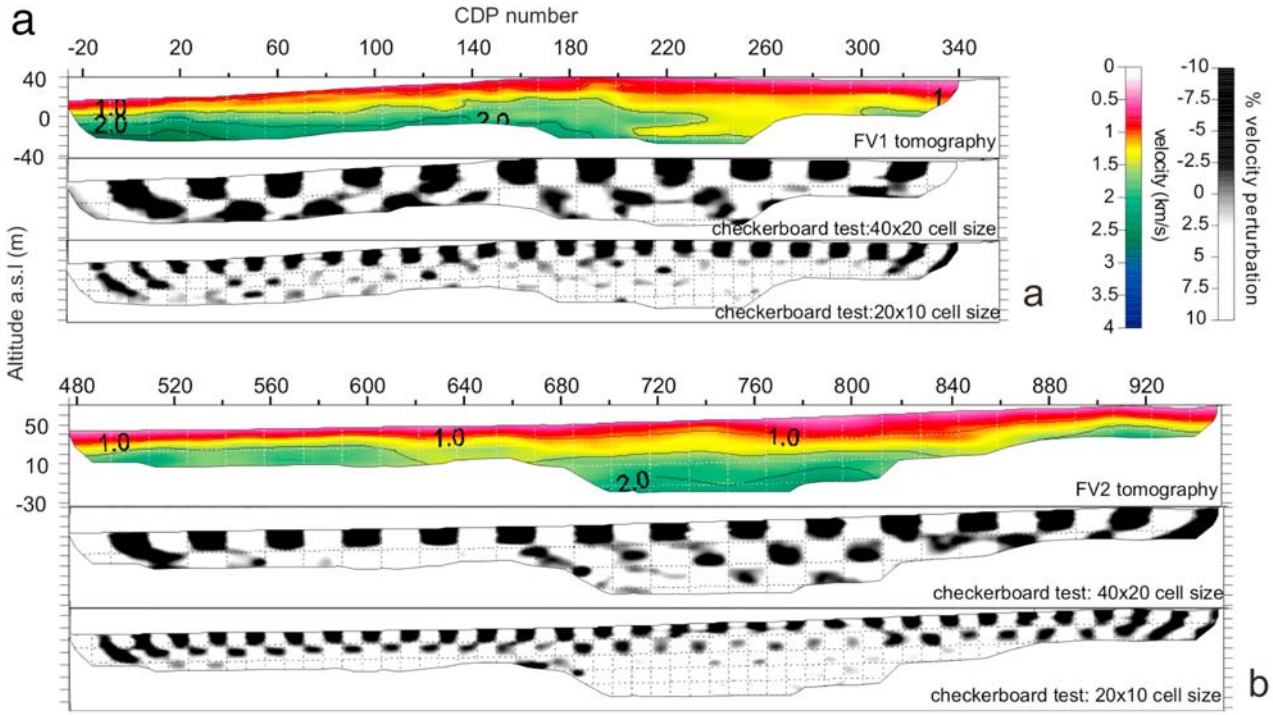

Figure 6. (a) FV1 and (b) FV2 final tomographic images and associated checkerboard tests. The region not sampled by raypaths is blank. (top) Tomographic images, (middle) perturbation retrieved after the a posteriori checkerboard resolution test with a 40 × 20 m cell, and (bottom) perturbation retrieved with a 20 × 10 m cell. The velocity perturbation for both tests is ±10%.

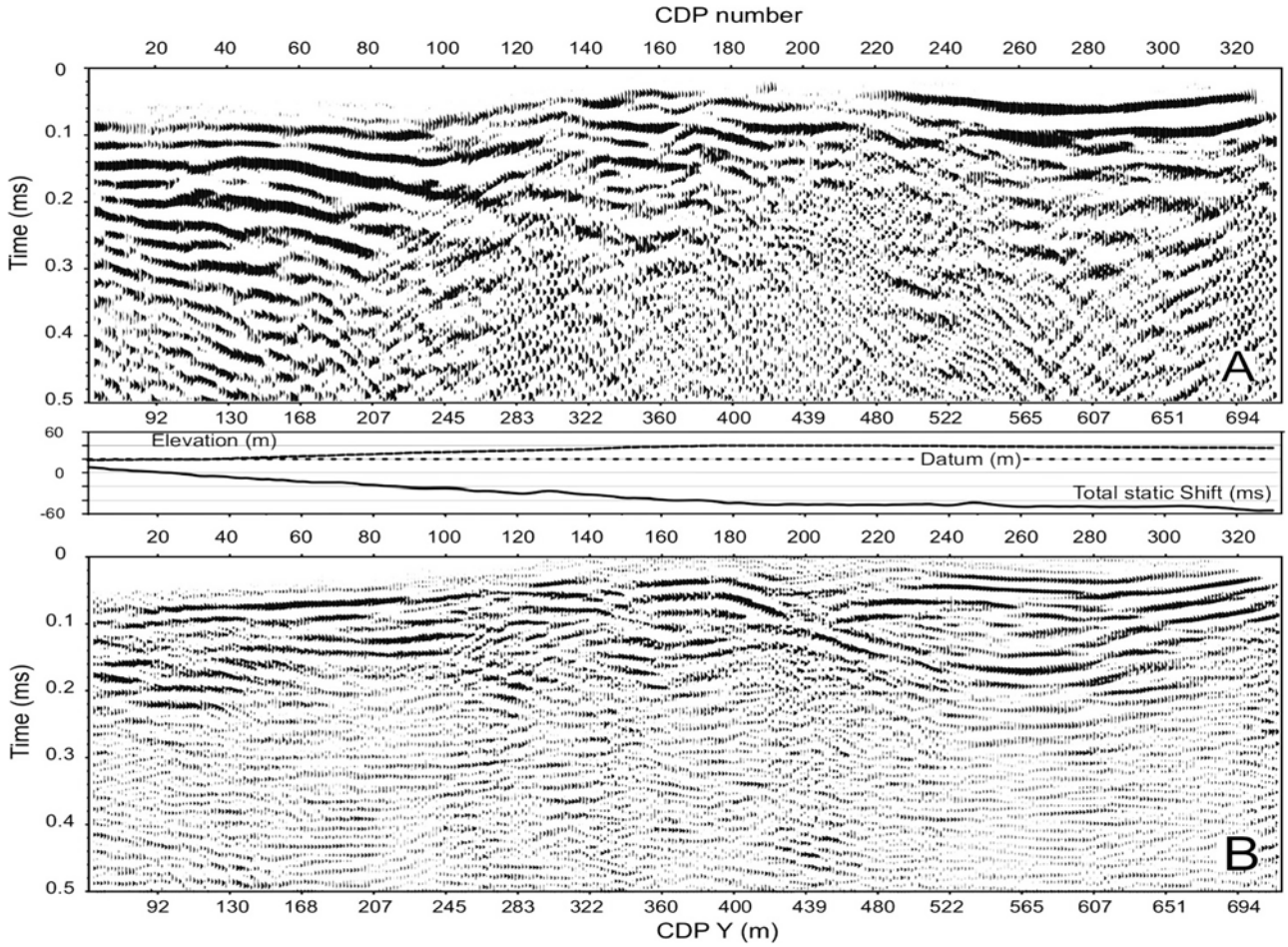

Figure 7. Comparison of results of FV1 line. (a) Stack section from a conventional processing sequence. (b) Stack section from an alternative sequence consisting mainly of (1) FDSD before spiking and predictive deconvolution, (2) surface consistent static corrections made using the tomography outcomes of Figure 6, and (3) integration of tomography within velocity analysis.

using the lower 50% of the eigenimages. Then frequency-spatial (F-X) deconvolution further increases the signal-to-noise (S/N) ratio. In the F-X deconvolution process, a complex prediction filter is used to predict the signal one trace ahead, across the frequency slice. Any difference between the predicted waveform and the actual one can be classified as noise and removed.

[16] A 2-D Kirchhoff poststack depth migration was finally applied to the data. This algorithm performs a migration by applying a Green's function to each CDP location using a traveltime map. Traveltime maps relate time and amplitude from each surface location to a region of points in the subsurface. For this migration we used a vertically and laterally variant interval velocity field, $V_{INT}(x, z)$, obtained by integrating our tomographic and semblance data, which were then converted in interval velocity and smoothed. Kirchhoff depth migration provides good handling of steep dips up to and beyond 90°, that is, turning ray energy. This is highly desirable in volcanic environments, which are generally characterized by extreme dips. For traveltime map computation we employed a multiple-arrival ray tracing technique, which uses up to five arrivals of significant energy to compute traveltime.

[17] Comparisons between stack sections obtained with the alternative seismic processing sequence and the conventional processing are reported in Figures 7 and 8. The improved stack sections have a better S/N ratio and higher frequencies and allow seeing, with higher detail, features which are unclear on the other sections. In particular, it is evident that FDSD enhanced the performance of minimum phase spiking and predictive deconvolution, as clearly visible in Figure 7 where multiples and ringing are effectively reduced. The imaging improvement is particularly evident on Figure 7a, CDPs 120–220, where a feature resembling in shape and dimension some offshore mud volcanoes is clearly visible [*Yusifov and Rabinowitz*, 2004]. However, the well-organized, inner reflective structure of such a body is recovered only by the use of alternative techniques (Figure 7b). A similar discussion can be made for the antiform structure imaged in Figure 8 (CDPs 700–880).

4. Description of the Results

[18] Interpretation of the seismic section benefits from the information provided by two geothermal exploratory wells drilled by Azienda Generale Italiana Petroli (AGIP), Ente

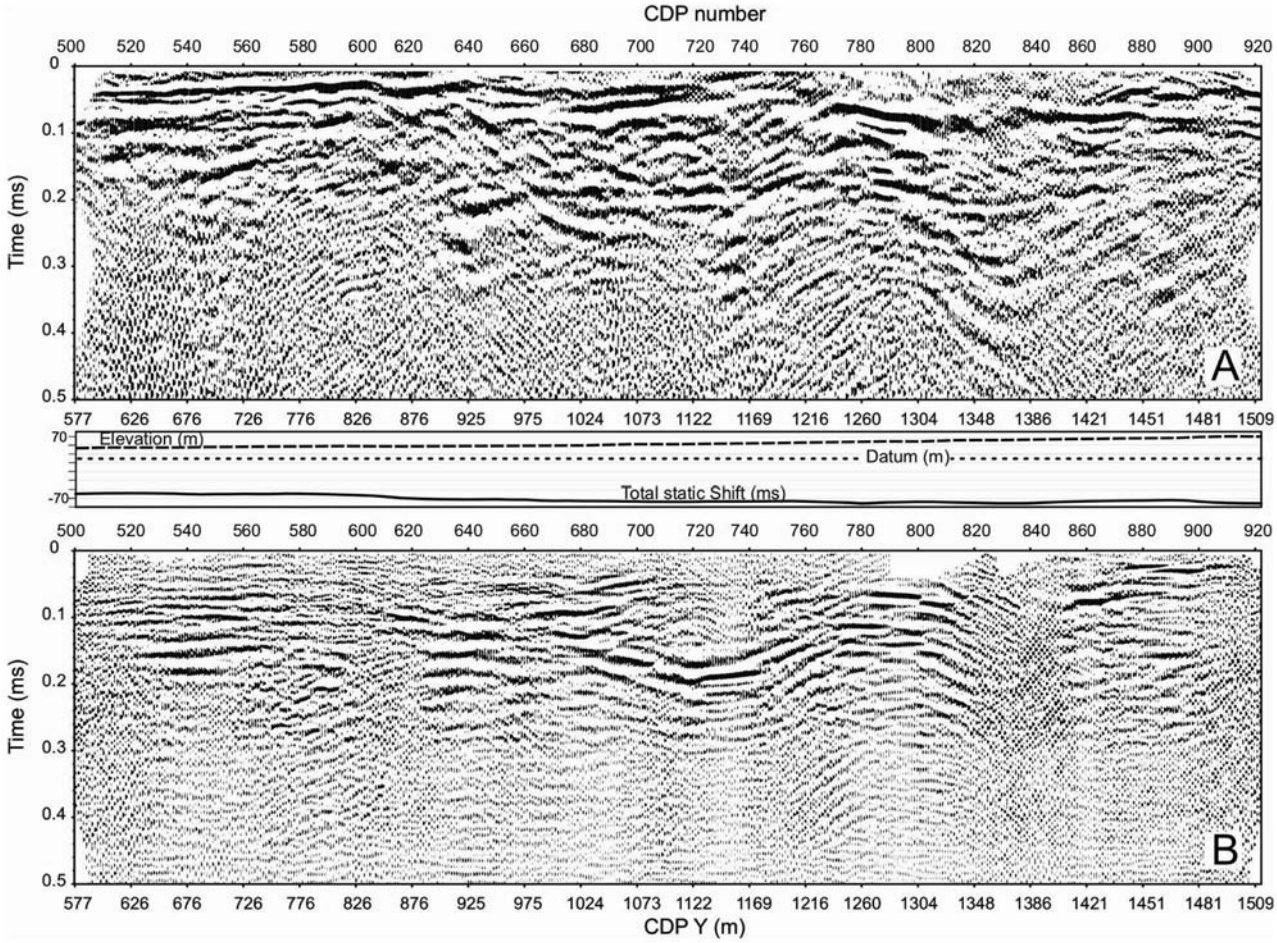

Figure 8. Comparison of results of FV2 line. (a) Stack section from a conventional processing sequence. (b) Stack section from an alternative sequence consisting mainly of (1) FDSD before spiking and predictive deconvolution, (2) CDP binning using crooked line geometry, (3) surface consistent static corrections made using the tomography outcomes of Figure 5, and (4) integration of tomography within velocity analysis.

Nazionale per l'Energia Elettrica (ENEL), and Electrica Muntenia Sud (EMS) during the 1980s inside La Fossa Caldera [*Gioncada and Sbrana*, 1991]. Well IV1 is located to the SW of La Fossa Caldera (see Figure 1b, about 200 m from the southern end of line FV2) and reaches a maximum depth of 2050 m. Well VP1 is 1000 m deep and is positioned about 300 m to the east of the northernmost point of profile FV1. Unfortunately, geophysical logs for these wells are not available to us. We also used the surface geology information [*De Astis et al.*, 2006] as a constraint for seismic interpretation.

[19] Stratigraphically, we define four main seismic sequences, bounded by three unconformities. Units A and B of Figure 9 have been associated to sequences of pyroclastic and reworked deposits outcropping in the study area [*De Astis et al.*, 2006]. We divide unit B into three subunits: B_1 shows parallel and continuous reflection configurations, probably indicative of pyroclastic flows/fall/lava sequences. We recognized a dome-shaped body B_2 accreted directly above the top of unconformity 2 (Figure 9, CDPs 120–240), with a diameter of about 300 m and a relief of 50–60 m. This body shows a well-organized internal structure and matches with seismic activity beneath B_2 at about 1 km deep (S. Gambino, unpublished data, 2007) and with a peak of CO_2 flux rate, measured in the area by *Diliberto et al.* [2002]. According to these evidences, B_2 may likely represent a small cooling eccentric vent made up of highly fractured lava which allows the upraising of gas to the surface. B_2 can also be interpreted as a small hyaloclastite mound. Reflectors pertaining to seismic units A and B_1 show clear onlap terminations above body B_2; in case of a simple sedimentary environment, onlaps are an obvious age indicator (i.e., A younger than B_2). However, the bending of units A and B_1 above B_2 gives a different age indication (i.e., B_2 younger than A). Even if we do not take into account the velocity pull-up caused by B_2, in volcanic environments this bending can be explained by the fact that fallout and flow deposits are influenced by the preexisting morphology. Seismic tomography is consistent with reflection data as it shows an increase of velocity along the upper part of unit B_2 (Figure 6, CDPs 120–220). The velocity anomaly has an overall pattern fitting the arch-shaped B_2 on the seismic section, and subunit B_3 is highly hypothetic as it is based on a possible onlap of B_1 over B_3 on the left end of

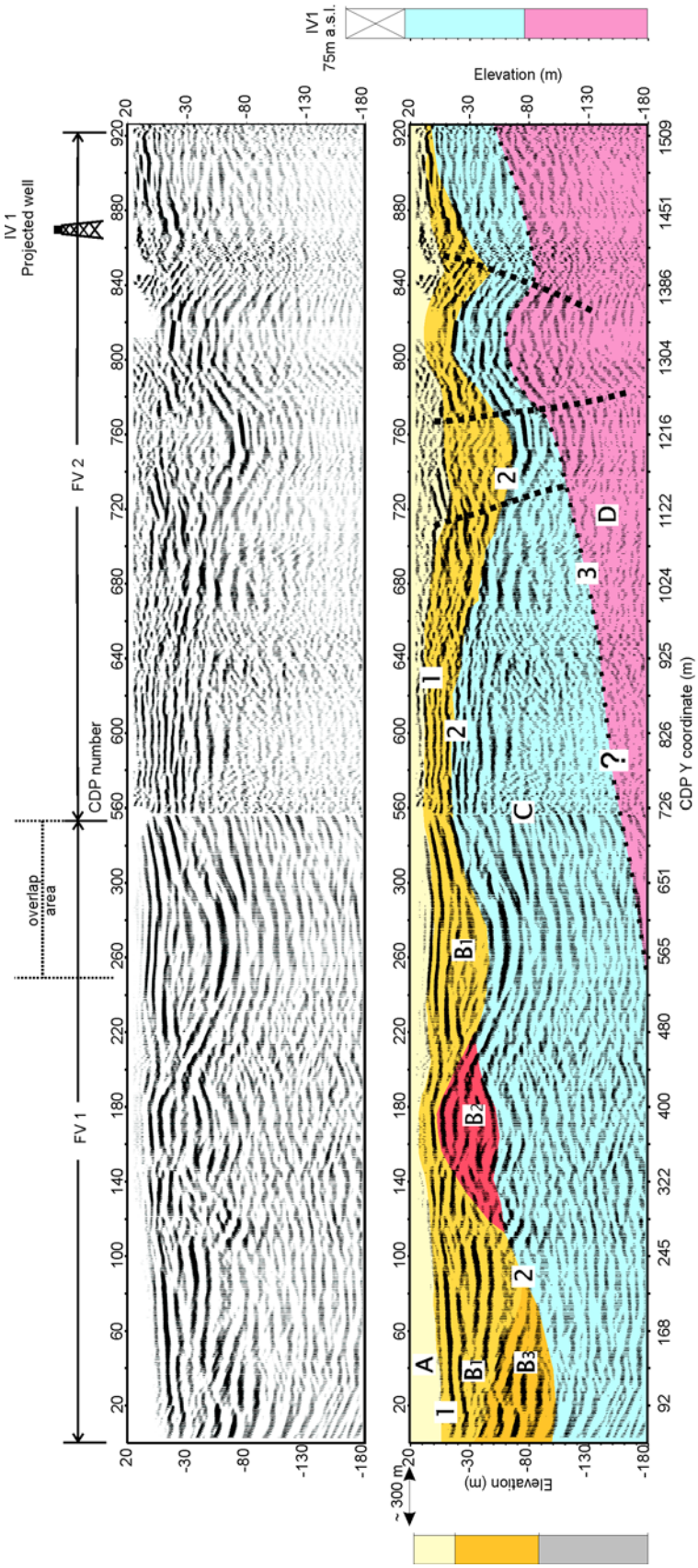

Figure 9. (top) Kirchhoff depth migrated data. The composite line was obtained by merging the end of line FV1 with line FV2, which was cut at CDP 550. The two lines do not overlap perfectly (see Figure 4); however, in the merging area the altitude difference and their relative distance are minimal; therefore, reflectivity differences are negligible. (bottom) Interpreted merged section with location and stratigraphy.

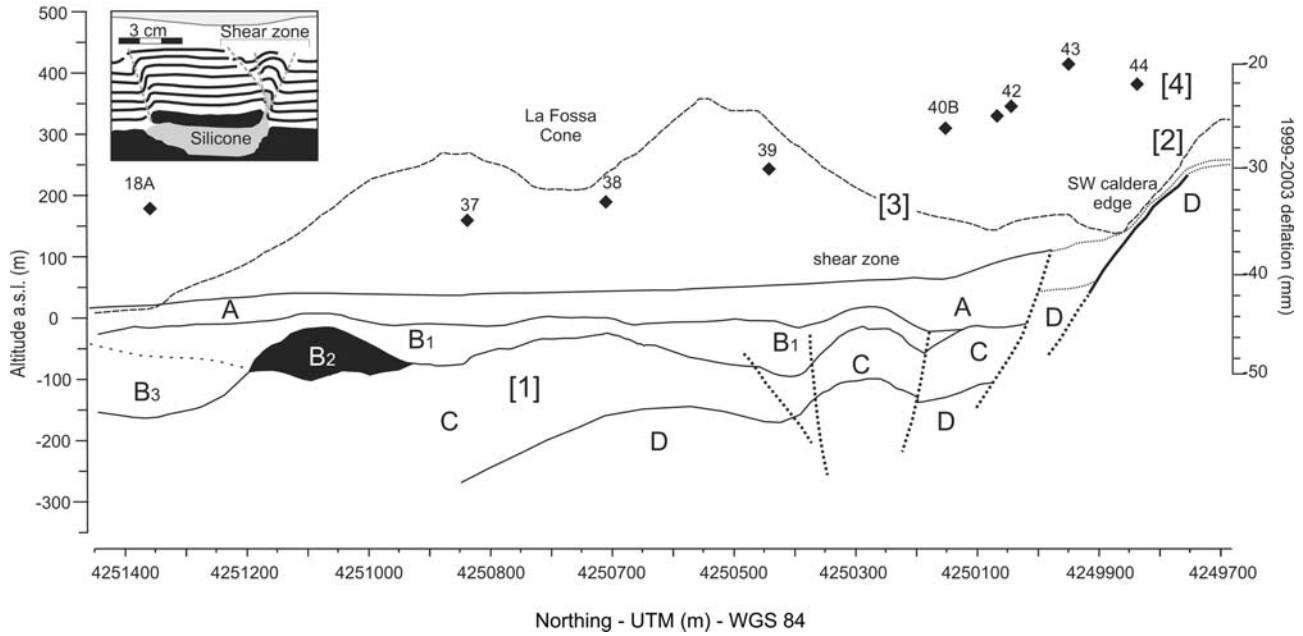

Figure 10. Conceptual model of the deformation of the SW sector of La Fossa Caldera projected on the longitude axis of Figure 1b. Numbers in brackets indicate 1, schematic and projected interpretation from migrated seismic line compared with, 2, surface geology of SW boundary of La Fossa Caldera from projected cross section of *De Astis et al.* [2006]; 3, topography pattern along the cross section of *De Astis et al.* [2006] projected on the longitude; 4, ground leveling variations in the period 1999–2003 [*Obrizzo et al.*, 2004], acquired along a profile coincident with the seismic data and also projected on the longitude. The reactivated structures, found at UTM metric coordinate 450300, are about 750 m from the projected caldera edge. Inset shows an analogical model showing a section view of the final stage of development of collapse after doming (modified from *Acocella et al.* [2000]). The asymmetry in the model shows that during collapse most of the reactivation occurs in correspondence of the previous structures. The shear zone is intruded by silicone (which simulates magma) at depth. Reprinted with permission from Elsevier.

the section. Because of low CDP coverage at the extremes, this effect can also be caused by stacking of coherent noise.

[20] The top of unit C is marked by a clear reflector (unconformity 2). However, S/N ratio starts to decrease within this unit; therefore, the reflection configuration is unclear. On the basis of well information, C may be interpreted as a hyaloclastite layer. Unconformity 3, visible only on the right-hand side of Figure 9, can instead represent the contact with the intracaldera lavas and welded scoriae (unit D in Figure 9). However, the top of this lava sequence is also highly hypothetical on the basis of our data, and it has been interpreted using both well information and the outcomes of the tomography experiment of *Chiarabba et al.* [2004], which evidences a shallow high *P* wave velocity body in the depth range pertaining to seismic unit D. The main structural feature of this profile is the evidence of compressive deformation at CDPs 760–840. Reflectors appear bended with an anticline-like pattern. Bending also involves the younger reflectors, being indicative of recent deformation. A pair of inward dipping, high-angle reverse faults delimits this area.

5. Discussion and Conclusions

[21] The seismic reflection method, applied to volcanic environments, may provide important information on the inner structure of calderas if the acquisition and processing are modified from the standard techniques used in simpler geological settings. Good quality seismic data, available for integration with other geophysical and geological surveys, are fundamental to improving the shallow subsurface exploration of key volcanic areas, whereas other methods are hampered by logistic and geological conditions, such as electric resistivity, which suffers from saltwater contamination of the subsurface of La Fossa [*Revil et al.*, 2008]. Our seismic survey targeted the western side La Fossa Caldera, a site extremely challenging for testing acquisition and processing high-resolution seismic reflection techniques (e.g., Figure 2). Here effective removal of source-generated noise and precise estimation of near-surface stacking velocity are decisive for obtaining good quality stacks.

[22] Within La Fossa Caldera we discovered, in an area with anomalous CO_2 degassing, an eccentric vent or hyaloclastite mound showing a well-organized internal reflectivity configuration. Similar structures are also described "offshore" by *Davies et al.* [2002], on Paleogene dike-fed submarine volcanoes from the northeast Atlantic margin. In the southernmost part of the profile, deformation is consistent with resurgent doming (Figure 10) [*Acocella et al.*, 2000]. In detail, seismic data show an asymmetrical anticline delimited by a pair of inward dipping, high-angle reverse faults. Those features are very similar to the analog

models of caldera collapse after doming described by *Acocella et al.* [2000], who also observed a complete reactivation, with opposite kinematics, of the preexisting bounding faults during the inversion of the deformation. Those faults in the analog model of *Acocella et al.* [2000] formed as high-angle reverse faults during resurgence and are reactivated as subvertical normal faults during caldera collapse modeling. The seismic feature highlighted by our seismic profiling can therefore be interpreted as an intracaldera shear zone delimiting two sectors of La Fossa with different uplift-deflation gradients, as is reasonable in a polyphase caldera [*De Astis et al.*, 2006] (see sketch in Figure 10). This interpretation is also in good agreement with recent ground leveling [*Obrizzo et al.*, 2004], which shows a flexure of the 1999–2003 vertical deformation pattern in correspondence to the antiform structure. The possible presence of a weakness zone (i.e., a shear zone characterized by high mechanical stress) within the caldera should be taken into account for assessing the volcanic hazard of La Fossa.

[23] **Acknowledgments.** We thank Francesco Varriale for his valuable help with the preparation of the manuscript and figures. The comments and suggestions of Luigi Improta, Guido Ventura, and an anonymous reviewer allowed us to improve the article. The authors would like to acknowledge the help and cooperation of Paolo Gasparini and Roberto Muti of AMRA S.c. a r.l. for help in coordinating the data acquisition with the Minivib and are also grateful to Anna Cicchella, Imma Correale, Dario De Rosa, Vincenzo Di Fiore, and Lucia Occorsio for their valuable help during the hard field work. The collaboration of Antonio Rapolla and CUGRI, in providing part of the instrumentation, is kindly acknowledged. Research support by INGV-DPC 2005-2007 V3_5_03 to P.P.G. Bruno.

References

Ackermann, H. D., L. W. Pankratz, and D. Dansereau (1986), Resolution of ambiguities of seismic refraction traveltime curves, *Geophysics*, *51*, 223–235, doi:10.1190/1.1442082.

Acocella, V., F. Cifelli, and R. Funiciello (2000), Analogue models of collapse calderas and resurgent domes, *J. Volcanol. Geotherm. Res.*, *104*, 81–96, doi:10.1016/S0377-0273(00)00201-8.

Baldi, P., S. Bonvalot, P. Briole, and M. Marsella (2000), Digital photogrammetry and kinematic GPS for monitoring volcanic areas, *Geophys. J. Int.*, *142*(3), 801–811, doi:10.1046/j.1365-246x.2000.00194.x.

Barberi, P., F. Gasparini, F. Innocenti, and L. Villari (1973), Volcanism of the southern Tyrrhenian Sea and its geodynamic implications, *J. Geophys. Res.*, *78*(23), 5221–5232, doi:10.1029/JB078i023p05221.

Barberi, F., A. Gandino, A. Gioncada, P. La Torre, A. Sbrana, and C. Zenucchini (1994), The deep structure of the Eolian arc (Filicudi-Panarea-Vulcano sector) in light of gravity, magnetic and volcanological data, *J. Volcanol. Geotherm. Res.*, *61*, 189–206, doi:10.1016/0377-0273(94)90003-5.

Berrino, G. (2000), Combined gravimetry in the observation of volcanic processes in Italy, *J. Geodyn.*, *30*, 371–388, doi:10.1016/S0264-3707(99)00072-1.

Blanco-Montenegro, I., R. De Ritis, and M. Chiappini (2007), Imaging and modelling the subsurface structure of volcanic calderas with high-resolution aeromagnetic data at Vulcano (Aeolian Islands, Italy), *Bull. Volcanol.*, *69*, 643–659, doi:10.1007/s00445-006-0100-7.

Brittle, K. F. (2001), Vibroseis deconvolution: Frequency-domain methods, M.S. thesis, Dep. of Geol. and Geophys., Univ. of Calgary, Calgary, Alberta, Canada.

Castellet y Ballarà, G., R. Crescenzi, A. Pompili, and R. Triglia (1982), A petrological model on magma evolution of Vulcano eruptive complex (Aeolian Islands—Italy), in *The Comparative Study of the Planets: Proceedings of the NATO Advanced Study Institute Held at Vulcano (Aeolian Islands), Italy, September 14–25, 1981*, edited by A. Coradini and M. Fulchignoni, pp. 459–476, D. Reidel, Dordrecht, Holland.

Chiarabba, C., N. A. Pino, G. Ventura, and G. Vilardo (2004), Structural features of the shallow plumbing system of Vulcano Island Italy, *Bull. Volcanol.*, *66*, 477–484, doi:10.1007/s00445-003-0331-9.

Chiodini, G., R. Cioni, S. Falsaperla, A. Montalto, M. Guidi, and L. Marini (1992), Geochemical and seismological investigations at Vulcano (Aeolian Islands) during 1978–1989, *J. Geophys. Res.*, *97*, 11,025–11,032, doi:10.1029/92JB00518.

Continisio, R., F. Ferrucci, G. Gaudiosi, D. Lo Bascio, and G. Ventura (1997), Malta escarpment and Mt. Etna: Early stages of an asymmetric rifting process? Evidences from geophysical and geological data, *Acta Vulcanol.*, *9*, 39–47.

Davies, R., B. R. Bell, J. A. Cartwright, and S. Shoulders (2002), Three-dimensional seismic imaging of Paleogene dike-fed submarine volcanoes from the northeast Atlantic margin, *Geology*, *30*, 223–226, doi:10.1130/0091-7613(2002)030<0223:TDSIOP>2.0.CO;2.

De Astis, G., L. La Volpe, A. Peccerillo, and L. Civetta (1997), Volcanological and petrological evolution of Vulcano Island (Aeolian Arc, southern Tyrrhenian Sea), *J. Geophys. Res.*, *102*, 8021–8050, doi:10.1029/96JB03735.

De Astis, G., A. Peccerillo, P. D. Kempton, L. La Volpe, and T. W. Wu (2000), Transition from calc-alkaline to potassic magmatism in subduction environments: Geochemical and Sr, Nd, Pb isotopic constraints from the island of Vulcano (Aeolian arc), *Contrib. Mineral. Petrol.*, *139*, 684–703, doi:10.1007/s004100000172.

De Astis, G., P. Dellino, L. La Volpe, F. Lucchi, and C. A. Tranne (2006), Geological map of the island of Vulcano (Aeolian Islands) scale 1:10000, edited by L. La Volpe and G. De Astis, Litografia Artistica Cartogr., Florence, Italy.

Dell'Aversana, P., E. Ceragioli, S. Morandi, and A. Zollo (2000), A simultaneous acquisition test of high-density 'global offset' seismic in complex geological settings, *First Break*, *18*, 87–96, doi:10.1046/j.1365-2397.2000.00053.x.

Diliberto, S. I., S. Gurrieri, and M. Valenza (2002), Relationships between diffuse CO_2 emissions and volcanic activity on the island of Vulcano (Aeolian Islands, Italy) during the period 1984–1994, *Bull. Volcanol.*, *64*, 219–228, doi:10.1007/s00445-001-0198-6.

Doll, W. E., R. D. Miller, and J. Xia (1998), A noninvasive shallow seismic source comparison on the Oak Ridge Reservation, Tennessee, *Geophysics*, *63*, 1318–1331, doi:10.1190/1.1444433.

Finetti, I., and A. Del Ben (1986), Geophysical study of the Tyrrhenian opening, *Bol. Geofis. Teor. Appl.*, *28*, 75–155.

Frazzetta, G., G. Lanzafame, and L. Villari (1982), Deformazioni e tettonica attiva a Lipari e Vulcano (Eolie), *Mem. Soc. Geol. Ital.*, *24*, 293–297.

Frazzetta, G., G. La Volpe, and M. F. Sheridan (1983), Evolution of the Fossa Cone, Vulcano, *J. Volcanol. Geotherm. Res.*, *17*, 329–360, doi:10.1016/0377-0273(83)90075-6.

Furukawa, R., S. Nakano, S. Okuma, and M. Sugihara (2001), Visiting Cratere; Brief geologic survey at Vulcano Island, Italy, *Chishitsu News*, *559*, 32–40.

Ghisetti, F. (1979), Relazioni tra strutture e fasi trascorrenti e distensive lungo i sistemi Messina-Fiumefreddo, Tindari–Letoianni e Alia-Malvagna-Sicilia nord-orientale: Uno studio microtettonico, *Geol. Rom.*, *18*, 23–58.

Gioncada, A., and A. Sbrana (1991), "La Fossa Caldera", Vulcano: Inferences from deep drillings, *Acta Vulcanol.*, *1*, 115–126.

Gioncada, A., R. Mazzuoli, M. Bisson, and M. T. Pareschi (2003), Petrology of volcanic products younger than 42 ka on the Lipari-Vulcano complex (Aeolian Islands, Italy): An example of volcanism controlled by tectonics, *J. Volcanol. Geotherm. Res.*, *122*, 191–220, doi:10.1016/S0377-0273(02)00502-4.

Granieri, D., M. L. Caparezza, G. Chiodini, R. Avino, S. Caliro, M. Ranaldi, T. Ricci, and L. Tarchini (2006), Correlated increase in CO_2 fumarolic content and diffuse emission from La Fossa crater (Vulcano, Italy): Evidence of volcanic unrest or increasing gas release from a stationary deep magma body, *Geophys. Res. Lett.*, *33*, L13316, doi:10.1029/2006GL026460.

Hammer, P. T. C., R. M. Clowes, and K. Ramachandran (2004), High-resolution seismic reflection imaging of a thin, diamondiferous, kimberlite dyke, *Geophysics*, *69*, 1143–1154, doi:10.1190/1.1801932.

Improta, L., and P. P. Bruno (2007), Combining seismic reflection with multifold wide-aperture profiling: An effective strategy for high-resolution shallow imaging of active faults, *Geophys. Res. Lett.*, *34*, L20310, doi:10.1029/2007GL031893.

Jin, S., and R. Madariaga (1994), Nonlinear velocity inversion by a two-step Monte Carlo method, *Geophysics*, *59*, 577–590, doi:10.1190/1.1443618.

Karhunen, J. (1984), Adaptive algorithms for estimating eigenvectors of correlation type matrices, *Proc. ICASSP*, *9*, 592–595.

Kasahara, K., F. Yamamizu, A. Takahashi, and T. Ikawa (1991), Reflection profiles of the active seismic and volcanic region off the east coast of Izu Peninsula, *J. Phys. Earth*, *39*(1), 361–370.

Keller, J. (1974), Petrology of some volcanic rock series of the Aeolian Arc, southern Tyrrhenian Sea: Calc-alkaline and shoshonitic associations, *Contrib. Mineral. Petrol.*, *45*, 29–47, doi:10.1007/BF00377991.

Keller, J. (1980), The island of Vulcano, *Rend. Soc. Ital. Mineral. Petrol.*, *36*(1), 369–414.

Keller, J. (1982), Mediterranean island arcs, in *Andesites: Orogenic Andesites and Related Rocks*, edited by R. S. Thorpe, pp. 307–325, John Wiley, Chichester, U. K.

Larsen, G., P. Hewitt, and A. Siewert (2007), Correlating versus inverting Vibroseis records: Recovering what you put into the ground, paper presented at 2007 CSPG CSEG Convention, Can. Soc. of Pet. Geol., Calgary, Alberta, Canada, 14–17 May.

Makris, J., and J. Thiessen (1984), Wide-angle reflections: A tool to penetrate horizons with high acoustic impedance contrasts, paper presented at SEG 54th Annual Meeting, Soc. of Explor. Geophys., Atlanta, Ga.

Mazzotti, A. P., E. Stucchi, G. L. Fradelizio, L. Zanzi, and P. Scandone (2000), Seismic exploration in complex terrains: A processing experience in the Southern Apennines, *Geophysics*, *65*, 1402–1417, doi:10.1190/1.1444830.

Nakanishi, I., and K. Yamaguchi (1986), A numerical experiment on nonlinear image reconstruction from the first-arrival times for two-dimensional island arc structure, *J. Phys. Earth*, *34*, 195–201.

Obrizzo, F., G. Brandi, and M. Dolce (2004), Isola di Vulcano (Isole Eolie) movimenti verticali del suolo: Livellazione di precisione Ottobre 2003, *INGV Open File Rep. 1*, Natl. Inst. of Geophys. and Volcanol., Rome.

Okuma, S., T. Nakatsuka, M. Komazawa, M. Sugihara, S. Nakano, R. Furukawa, and R. Supper (2006), Shallow subsurface structure of the Vulcano-Lipari volcanic complex, Italy, constrained by helicopter-borne aeromagnetic surveys, *Explor. Geophys.*, *37*, 129–138, doi:10.1071/EG06129.

Operto, S., C. Ravaut, L. Improta, J. Virieux, A. Herrero, and P. Dell'Aversana (2004), Quantitative imaging of complex structures from dense wide-aperture seismic data by multiscale traveltime and waveform inversions: A case study, *Geophys. Prospect.*, *52*(6), 625–651, doi:10.1111/j.1365-2478.2004.00452.x.

Privitera, E. (1997), La sismicità di Vulcano e delle aree limitrofe: Contributi alla definizione dell'assetto strutturale, in *Progetto Vulcano: Risultati delle Attività di Ricerca 1993–1995*, pp. 258–263, Felici, San Giuliano Terme, Italy.

Reshef, M., H. Shulman, and Z. Ben-Avraham (2003), A case study of sub-basalt imaging in land region covered with basalt flows, *Geophys. Prospect.*, *51*(3), 247–260, doi:10.1046/j.1365-2478.2003.00368.x.

Revil, A., et al. (2008), Inner structure of La Fossa di Vulcano (Vulcano Island, southern Tyrrhenian Sea, Italy) revealed by high-resolution electric resistivity tomography coupled with self-potential, temperature, and CO_2 diffuse degassing measurements, *J. Geophys. Res.*, *113*, B07207, doi:10.1029/2007JB005394.

Roth, M., and K. Holliger (1999), Inversion of source-generated noise in high-resolution seismic data, *Leading Edge*, *18*, 1402–1406, doi:10.1190/1.1438230.

Scales, J. A. (1987), Tomography inversion via conjugate gradient method, *Geophysics*, *52*, 179–185, doi:10.1190/1.1442293.

Spitzer, R., F. O. Nitsche, and A. G. Green (2001), Reducing source-generated noise in shallow seismic data using linear and hyperbolic $\tau - p$ transformations, *Geophysics*, *66*, 1612–1621, doi:10.1190/1.1487106.

Supper, R., R. De Ritis, K. Motschka, and M. Chiappini (2004), Aeromagnetic anomaly images of Vulcano and southern Lipari Islands (Aeolian Archipelago, Italy), *Ann. Geophys.*, *47*(6), 1803–1810.

Ventura, G. (1994), Tectonics, structural evolution and caldera formation on Vulcano Island (Aeolian Archipelago, southern Tyrrhenian Sea), *J. Volcanol. Geotherm. Res.*, *60*, 207–224, doi:10.1016/0377-0273(94)90052-3.

Yusifov, M., and P. Rabinowitz (2004), Classification of mud volcanoes in the south Caspian basin, offshore Azerbaijan, *Mar. Pet. Geol.*, *21*, 965–975, doi:10.1016/j.marpetgeo.2004.06.002.

P. P. G. Bruno, Sezione Osservatorio Vesuviano, Istituto Nazionale di Geofisica e Vulcanologia, Via Diocleziano, 328, I-80124 Napoli, Italy. (bruno@gm.ingv.it)

A. Castiello, Sezione Sismologia e Tettonofisica, Istituto Nazionale di Geofisica e Vulcanologia, Via di Vigna Murata, 605, I-00143 Roma, Italy.